Dynamic Pathways for Viral Capsid Assembly

Michael F. Hagan and David Chandler*

Department of Chemistry, University of California, Berkeley, CA 94720

(Dated: November 7, 2005)

We develop a class of models with which we simulate the assembly of particles into T1 capsid-like objects using Newtonian dynamics. By simulating assembly for many different values of system parameters, we vary the forces that drive assembly. For some ranges of parameters, assembly is facile, while for others, assembly is dynamically frustrated by kinetic traps corresponding to malformed or incompletely formed capsids. Our simulations sample many independent trajectories at various capsomer concentrations, allowing for statistically meaningful conclusions. Depending on subunit (i.e., capsomer) geometries, successful assembly proceeds by several mechanisms involving binding of intermediates of various sizes. We discuss the relationship between these mechanisms and experimental evaluations of capsid assembly processes.

I. INTRODUCTION

This paper is devoted to introducing a simple class of capsomer models, and demonstrating that Newtonian dynamics of these models exhibit spontaneous assembly into 60-unit icosahedral capsids, depending upon conditions (i.e., particle concentration and force field parameters). We believe it is the first report of statistically meaningful simulations of capsid assembly that follow from unbiased dynamics obeying time-reversal symmetry and detailed balance.

The formation of viral capsids is a marvel of natural engineering and design. A large number (from 60 to thousands) of protein subunits assemble into complete, reproducible structures under a variety of conditions while avoiding kinetic and thermodynamic traps. Understanding the features of capsid components that enable such robust assembly could be important for the development of synthetic supra-nano assemblies. In addition, this knowledge is essential for the development of anti-viral drugs that inhibit capsid assembly or disassembly and could focus efforts to direct the making of highly specific drug delivery vehicles. These goals necessitate the ability to manipulate when and where capsids assemble and disassemble. Thus, we seek to determine what externally or internally controlled factors promote or alleviate dynamic frustration in the capsid assembly process. Although many viruses assemble with the aid of nucleic acids and scaffolding proteins, the first step toward this objective is to understand the inherent ability of subunit-subunit interactions to direct spontaneous assembly.

The equilibrium properties of viral capsids have been the subject of insightful theoretical investigations (e.g Refs. 1, 2, 3, 4, 5, 6) and the assembly process has been investigated in a number of experiments (e.g. Refs. 7, 8, 9, 10, 11, 12, 13, 14, 15), yet this process is still poorly understood for many viruses (e.g. Ref. 16). Assembly is difficult to analyze experimentally because most intermediates are transient. With single molecule techniques, it is now possible to directly probe intermediate structures. Each intermediate, however, is a member of a large ensemble of structures and pathways that comprise the overall assembly process. Formation of an intermediate requires collective binding events that are regulated by a tightly balanced competition of forces between individual subunits. It is difficult, with experiments alone, to parse these interactions for the factors that are critical to the assembly process. Thus, it is useful to have complementary computational models in which the effects of different interactions can be isolated and monitored.

Studying assembly through computation is challenging because short range subunit-subunit properties regulate the formation of overall structure. Binding and unbinding rates of individual subunits are orders of magnitude faster than the overall assembly times. Furthermore, these rates are controlled by interactions defined on atomic lengths, which are three orders of magnitude smaller than typical capsid sizes. Prior computational studies provide valuable insights that we build upon; in particular, Zlotnick pioneered a rate-equation description of assembly [17] and Berger and co-workers developed particle based methods [18]. Earlier studies, although an important foundation for our work, are limited in that they have been based upon pre-conceived pathways of assembly [17, 19, 20, 21, 22], or dynamics that did not obey detailed balance [18, 23, 24, 25], or dynamics that was anecdotal [23, 26, 27, 28]. These approaches can be useful and physical justifications for them can be made. Nevertheless, we seek to avoid these limitations in order to understand the nature of possible kinetic traps and the extent of ensembles of successful assembly events. In Section II, we present our class of models for capsid subunits. We evaluate the thermodynamic properties of this model in Section III, and then discuss the results of dynamical simulations in Section IV. By simulating assembly for many different values of system parameters, we vary the strength of the forces that either drive or thwart assembly. We identify regions of parameter space in which two forms of kinetic traps prevail and we elucidate processes by which dynamic frustration is avoided in other regions of parameter space.

II. MODEL

Capsomers. Capsid proteins typically have several hundred residues that fold into well defined shapes with specific interactions that lead to attractions between complementary

sides of nearby subunits. We imagine that by integrating over degrees of freedom, such as atomic coordinates, as capsid proteins fluctuate about their native states, one can arrive at a model in which subunits have excluded volume and asymmetric pairwise bonding interactions between complementary sides. Several models have been presented in which asymmetric subunits, the capsomers, are represented by conglomerates of spherically symmetric particles with varying interaction strengths [6, 23, 27, 28]. These approaches can describe complex excluded volume shapes. The approach we take here, however, is simpler, and motivated by the modeling described in Ref. 26. Specifically, we use only a single spherical excluded volume per capsomer, and we use internal bond vectors to capture the effects of protein shape and complementarity.

Our model capsomers are of three types: B_3, B_4 and B_5, which contain three, four and five internal capsomer bond vectors, respectively. These bond vectors, $\mathbf{b}_i^{(\alpha)}$, are pictured in Figure 1. The index α goes from 1 to n_b, where $n_b = 3$ for the B_3 model, $n_b = 4$ for the B_4 model, and so forth, and the index i goes from 1 to N, where N is the number of capsomers in the system. The vector $\mathbf{r}_i^{(\alpha)} = \mathbf{R}_i + \mathbf{b}_i^{(\alpha)}$ is the position of interaction site α on capsomer i, where $\mathbf{R}_i$ is the center of capsomer i. All bond vectors have the same magnitude, b. Within a capsomer frame of reference, the bond vectors are fixed rigidly. They move only because the capsomer translates and rotates. This is not to say that proteins do not fluctuate. Those fluctuations, we imagine, have been averaged over, i.e., integrated out of the model at the level we consider.
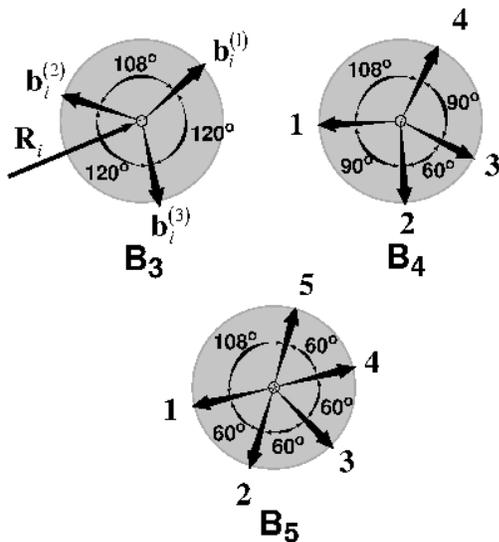

FIG. 1: Geometry of bond vectors in the B_3, B_4, and B_5 capsomer models. the center of capsomer i is at $\mathbf{R}_i$. The angles between indicated bond vectors within a capsomer are specified in degrees. They do not sum to $360° = 2\pi$ because the bond vectors are not coplanar.

The net potential energy of interaction among N capsomers, $U(1, 2, \ldots, N)$, is taken to be pair-decomposable,

$$U(1, 2, \ldots, N) = \sum_{i>j=1}^{N} u(i, j). \qquad (1)$$

where $u(i, j)$ depends upon the bond vectors and centers of capsomers i and j. The particular form for this pair potential depends upon which of the three models, B_3, B_4 or B_5 is under consideration. In each case, however, the potential is constructed so that the lowest energy configurations coincide with separate icosahedral clusters of 60 identical capsomers. These clusters represent capsids with triangulation number (T) of one [2]; for example, design B_5 is consistent with Fig. 3 of Ref 29. Our B_3 model is similar to the model considered in Ref. 26.

In each model, bond vectors or interaction sites have complementary counterparts. For example, in the B_3 model, interaction site pairs $(\alpha, \beta) = (1, 2)$ and $(3, 3)$ are the primary complementary pairs. This means that a favorable potential energy of interaction between a pair i and j of B_3 capsomers has two ways of occuring: 1) interaction site 1 on one capsomer overlaps with interaction site 2 on the other capsomer, and the respective bond vectors $\mathbf{b}_i^{(1)}$ and $\mathbf{b}_j^{(2)}$ are nearly antiparrallel; 2) interaction site 3 on one capsomer overlaps with interaction site 3 on the other, and $\mathbf{b}_i^{(3)}$ and $\mathbf{b}_j^{(3)}$ are nearly antiparrallel. The only favorable (i.e., attractive) interactions are those associated with primary complementary pairs.

In addition, there are secondary complementary pairs. For example, in the B_3 model, with primary complementary pair $(1,2)$, there is the secondary pair $(3,3)$. This means that a favorable interaction affected by the primary complementary pair $(1,2)$, as described in the previous paragraph, also requires that $\mathbf{b}_i^{(3)}$ and $\mathbf{b}_j^{(3)}$ are nearly coplanar. Similarly, for the primary complementary pair $(3,3)$, the secondary pair is either $(1,2)$ or $(2,1)$, meaning that if $\mathbf{b}_i^{(3)}$ and $\mathbf{b}_j^{(3)}$ are antiparallel, favorable interactions result only if $\mathbf{b}_i^{(1)}$ and $\mathbf{b}_j^{(2)}$ are nearly co-planar and $\mathbf{b}_i^{(2)}$ and $\mathbf{b}_j^{(1)}$ are nearly co-planar. Of course, because the capsomers are rigid bodies, $\mathbf{b}_i^{(1)}$ and $\mathbf{b}_j^{(2)}$ being co-planar implies $\mathbf{b}_i^{(2)}$ and $\mathbf{b}_j^{(1)}$ are co-planar. The primary and secondary pairs for each of the models are listed in the entrees to Table I. Local bonding associated with these complementarities and resulting capsid structures are illustrated in Figure 2. In creating these pictures, it is imagined that excluded volume interactions prohibit an interaction site from participating simultaneously in more than one favorable complementary interaction, as is the case for the models we describe.

The dependence of subunit-subunit interactions on the orientation of primary and secondary pairs incorporates the fact that there is a driving force for subunits to align complementary regions to maximize the contact between complementary residues. Capsid curvature in the minimum energy orientation arises from that fact that the angles between bond vectors on a given subunit do not sum to 2π.

Pair potential. The potential energy of interaction between

	Primary		Secondary			
	α	β	γ	ϵ	η	ν
B3	1	2	2	1	3	3
	2	1	1	2	1	2
	3	3	1	2	2	1
B4	1	4	2	3		
	2	3	1	4		
	3	2	4	1		
	4	1	3	2		
B5	1	5	5	1	2	4
	2	2	3	1	1	3
	3	4	2	5	4	3
	4	3	5	2	3	4
	5	1	1	5	4	2

$$\cos\left(\theta_{ij}^{(\alpha\beta)}\right) = -\mathbf{b}_i^{(\alpha)} \cdot \mathbf{b}_i^{(\beta)}/b^2 \qquad \mathbf{R}_{ij} = \mathbf{R}_i - \mathbf{R}_j$$

$$\cos\left(\phi_{ij}^{(\alpha\beta,1)}\right) = \frac{\left(\mathbf{b}_i^{(\gamma)} \times \mathbf{R}_{ij}\right) \cdot \left(\mathbf{R}_{ij} \times \mathbf{b}_i^{(\epsilon)}\right)}{\left|\mathbf{b}_i^{(\gamma)} \times \mathbf{R}_{ij}\right|\left|\mathbf{R}_{ij} \times \mathbf{b}_i^{(\epsilon)}\right|}$$

$$\cos\left(\phi_{ij}^{(\alpha\beta,2)}\right) = \frac{\left(\mathbf{b}_i^{(\eta)} \times \mathbf{R}_{ij}\right) \cdot \left(\mathbf{R}_{ij} \times \mathbf{b}_i^{(\nu)}\right)}{\left|\mathbf{b}_i^{(\eta)} \times \mathbf{R}_{ij}\right|\left|\mathbf{R}_{ij} \times \mathbf{b}_i^{(\nu)}\right|}$$

TABLE I: Primary and secondary complementary pairs and associated angles for the three capsomer models.
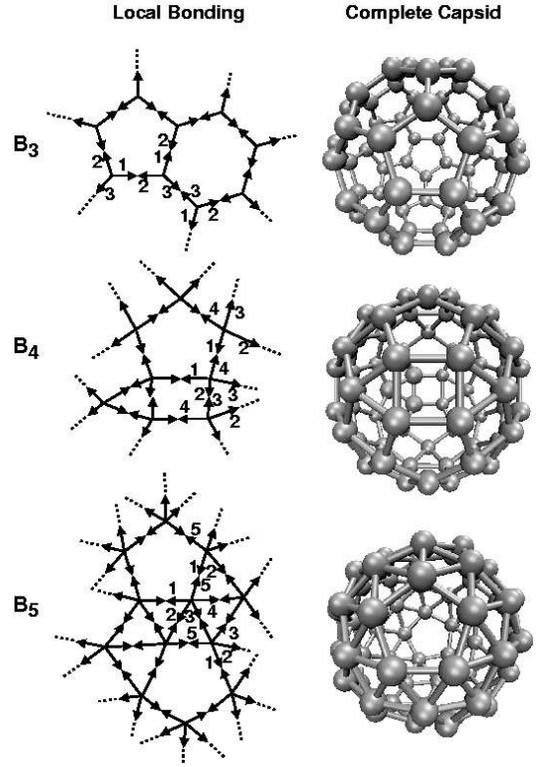

FIG. 2: Complementary pairs and bonding of capsomers. The first column specifies the model, the second illustrates the local bonding consistent with the complementary pairs of bond vectors, and the third illustrates the resulting complete capsid, with bonds depicting the attractive interactions resulting from complementary pairs. The pictures of complete capsids and all simulation snapshots shown in this work were generated in VMD [49]. The size of the spheres in these pictures has been reduced to aid visibility; parameters are chosen such that the minimum energy distance between neighboring capsomers is at the minimum in the WCA potential, Eq. 3.

two capsomers, say 1 and 2, is taken to have a spherically symmetric repulsive part, $u_0(|\mathbf{R}_2 - \mathbf{R}_1|)$, and an attractive part that depends upon both $\mathbf{R}_2 - \mathbf{R}_1$ and the bond vectors associated with the two capsomers,

$$\begin{aligned} u(1,2) &= u_0(|\mathbf{R}_2 - \mathbf{R}_1|) \\ &\quad + u_1\left(\mathbf{R}_2 - \mathbf{R}_1, \left\{\mathbf{b}_2^{(\alpha)}\right\}, \left\{\mathbf{b}_1^{(\gamma)}\right\}\right). \end{aligned} \quad (2)$$

For the repulsion, we have chosen the Weeks-Chandler-Andersen [30] potential,

$$\begin{aligned} u_0(R) &= 4\epsilon\left[(\sigma/R)^{12} - (\sigma/R)^6 + 1/4\right], \quad R < 2^{1/6}\sigma \\ &= 0, \quad R \geq 2^{1/6}\sigma. \end{aligned} \quad (3)$$

For the attractions we have chosen

$$\begin{aligned} &u_1\left(\mathbf{R}_2 - \mathbf{R}_1, \left\{\mathbf{b}_2^{(\sigma)}\right\}, \left\{\mathbf{b}_2^{(\gamma)}\right\}\right) \\ &= \sideset{}{'}\sum_{\alpha\beta} u_{\text{att}}\left(\left|\mathbf{r}_2^{(\sigma)} - \mathbf{r}_1^{(\beta)}\right|\right) s_{\alpha\beta}(1,2), \end{aligned} \quad (4)$$

where the primed sum is over primary complementary pairs,

$$\begin{aligned} u_{\text{att}}(r) &= 4\varepsilon_b\left[\left(\frac{\sigma}{r + 2^{1/6}\sigma}\right)^{12} - \left(\frac{\sigma}{r + 2^{1/6}\sigma}\right)^6 \right. \\ &\quad \left. - \left(\frac{\sigma}{r_c}\right)^{12} + \left(\frac{\sigma}{r_c}\right)^6\right], \quad r + 2^{1/6}\sigma < r_c \\ &= 0, \quad r + 2^{1/6}\sigma \geq r_c, \end{aligned} \quad (5)$$

which has its minimum value, $-\varepsilon_b$, when the separation of complementary pair interaction sites is zero, and $s_{\alpha\beta}(1,2)$ is the switching function, given by

$$\begin{aligned} s_{\alpha\beta}(1,2) &= \frac{1}{8}\left[\cos\left(\pi\theta_{12}^{(\alpha\beta)}/\theta_m\right) + 1\right] \\ &\quad \times \left[\cos\left(\pi\phi_{12}^{(\alpha\beta,1)}/\phi_m\right) + 1\right] \\ &\quad \times \left[\cos\left(\pi\phi_{12}^{(\alpha\beta,2)}/\phi_m\right) + 1\right] \end{aligned} \quad (6)$$

for models B_3 and B_5, and by

$$\begin{aligned} s_{\alpha\beta}(1,2) &= \frac{1}{4}\left[\cos\left(\pi\theta_{12}^{(\alpha\beta)}/\theta_m\right) + 1\right] \\ &\quad \times \left[\cos\left(\pi\phi_{12}^{(\alpha\beta,1)}/\phi_m\right) + 1\right] \end{aligned} \quad (7)$$

for model B_4. The angle variables used in these expressions are defined in Table I. Notice from that table, specifying a specific primary pair of complementary bonds prescribes specific corresponding secondary pairs. The switching function goes smoothly from 1 to 0 as the angle variables $\theta_{12}^{(\alpha\gamma)}$, $\phi_{12}^{(\alpha\gamma,1)}$

and $\phi_{12}^{(\alpha\gamma,2)}$ change from 0 to θ_m , ϕ_m and ϕ_m, respectively. Increase of these maximum angles θ_m and ϕ_m increases the configuration space in which two nearby subunits attract each other, but also weakens the driving force toward the minimum energy orientation.

Dynamical simulations Dynamical trajectories were calculated using Brownian dynamics, in which particle motions are calculated from Newton's laws with forces and torques arising from subunit-subunit interactions as well as drag and a random buffeting force due to the implicit solvent. We use the following coupled equations of motion

$$
\begin{aligned}
\dot{\mathbf{R}}_i &= \gamma\mathbf{F}_i + \delta\mathbf{F}_i \\
\boldsymbol{\omega}_i &= \gamma_r\boldsymbol{\tau}_i + \delta\boldsymbol{\tau}_i
\end{aligned}
\tag{8}
$$

where $\boldsymbol{\omega}$ is the angular velocity, the force is given by

$$
\mathbf{F}_i = -\partial U/\partial\mathbf{R}_i,
\tag{9}
$$

and the torque is given by

$$
\boldsymbol{\tau}_i = -\sum_\alpha \mathbf{b}_i^{(\alpha)} \times \left(\partial U/\partial\mathbf{b}_i^{(\alpha)}\right)
\tag{10}
$$

while $\delta\mathbf{F}_i$ and $\delta\boldsymbol{\tau}_i$ are a random force and torque, with covariances given by

$$
\begin{aligned}
\langle\delta\mathbf{F}_i(t)\delta\mathbf{F}_j(t')\rangle &= \mathbf{1}\delta(t-t')\delta_{ij}2k_BT/\gamma \\
\langle\delta\boldsymbol{\tau}_i(t)\delta\boldsymbol{\tau}_j(t')\rangle &= \mathbf{1}\delta(t-t')\delta_{ij}2k_BT/\gamma_r
\end{aligned}
\tag{11}
$$

where $\mathbf{1}$ is the identity matrix. The friction coefficients for translation and rotation are γ and γ_r, respectively, and k_BT is the thermal energy.

Parameter	Value	Definition
ϵ/k_BT	1	WCA energy parameter, Eq. 3
ε_b/k_BT	$9-22$	Attractive energy strength, Eq. 5
b/σ	$2^{-5/6}$	Bond vector length
$\gamma_r/\gamma\sigma^2$	0.4	Rotational friction coefficient, Eq. 8
ϕ_m (rad)	3.14	maximum dihedral angle, Eq. 6
θ_m (rad)	$0.1-3.0$	maximum bond angle, Eq. 6
L/σ	$11-100$	Simulation boxsize
N	1000	Number of subunits
$C_0 = N\sigma^3 L^{-3}$	$0.001-0.75$	Concentration of subunits
r_c/σ	2.5	Attractive energy cutoff distance
$\delta t/t_0$	0.006	Timestep
t_{obs}/t_0	6×10^5	Final observation time, 10^8 steps

TABLE II: Parameter values used for dynamical simulations in this work, where σ is the unit of length, k_BT is the thermal energy, γ is the translational friction constant, Eq. 8, and $t_0 \equiv \gamma\sigma^2/(48k_BT)$ is the unit time.

In our implementations of these equations, rigid body rotations were performed with quaternions [31] and rotational and translational displacements were calculated using the second order stochastic Runge-Kutta method [32, 33], as described in Appendix A. Periodic boundary conditions were used to simulate a bulk system. We employed reduced units in which the particle diameter $\sigma = 1$, k_BT is the unit of energy, and time

is scaled by $t_0 \equiv \gamma\sigma^2/(48k_BT)$. Each trajectory considered $N = 1000$ subunits and ran for 10^8 steps, usually with a time step of 0.006. The values of all parameters used in this work are documented in Table II. If units of length, σ, and temperature, T, are chosen to be $\sigma = 2$ nm and $T = 300$ K, the final observation time after 10^8 steps is $t_{obs} = 227.5$ μs, subunit concentrations, C_0 range from $2.08 \times 10^{-4} - 0.156$ mol/L, and binding energies, ε_b, range from $5.4 - 13.2$ kcal/mol.
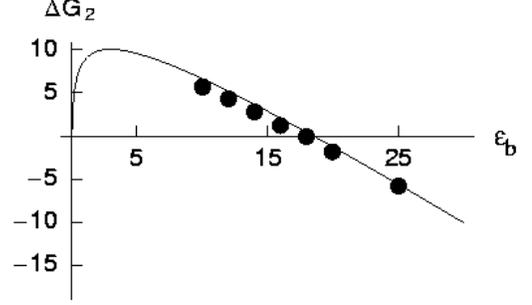

FIG. 3: Binding free energies for dimerization calculated from Eqs. 14,15 (line) and Monte Carlo simulations (points). Free energies are with reference to a standard state with volume fraction of 1 and free rotational motion, and the maximum angle parameters, defined in Eq. 6, are $\theta_m = \phi_m = 0.5$.
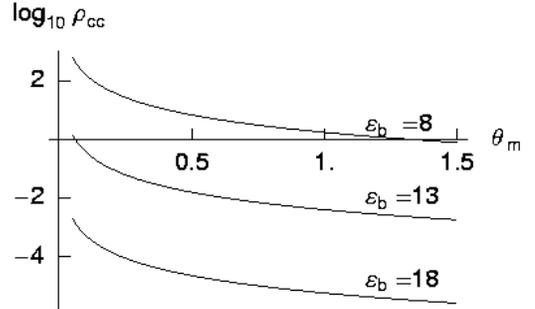

FIG. 4: The thermodynamic critical subunit concentration for capsid formation, ρ_{cc}, as calculated from Eqs 15, 16, and 17 for design B_3 and $\phi_m = \pi$. Above these subunit concentrations, most subunits will be found in complete capsids at equilibrium.

III. THERMODYNAMICS OF CAPSID ASSEMBLY

The equilibrium concentrations of free subunits (monomers) and capsid intermediates can be related by the law of mass action [34]

$$
\rho_n\sigma^3 = \left(\rho_1\sigma^3\right)^n \exp(-\beta\Delta G_n)
\tag{12}
$$

where ρ_n is the number density of an intermediate with n subunits, σ is the molecular dimension, $\beta = 1/k_BT$ is the inverse of the thermal energy, and ΔG_n is the driving force to form an intermediate of size n. The driving force for assembly comes from the fact that subunits experience a favorable
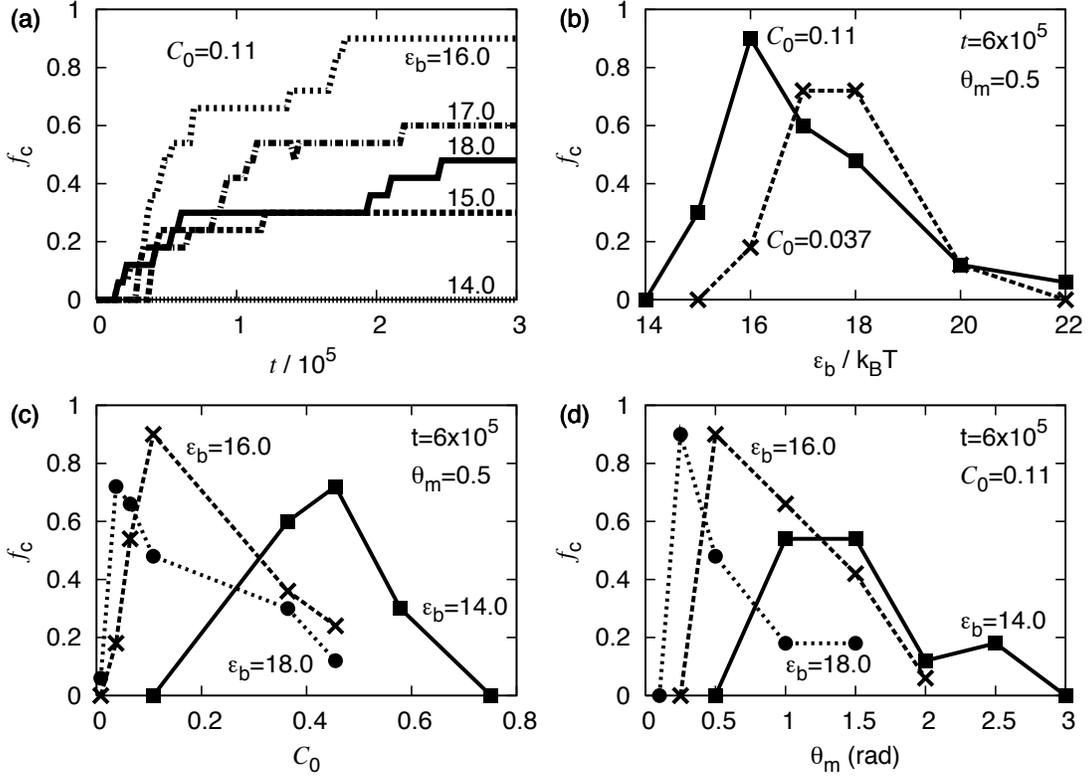
FIG. 5: Examples of the influence of system parameters on assembly dynamics for design B_3. (a) The fraction of complete capsids versus time, f_c, is shown for $\theta_m = 0.5$ and $C_0 = N\sigma^3/L^3 = 0.11$ at varying ε_b illustrating the sigmoidal shape of capsid yields. Note that variations of f_c are in discrete units of 0.06 because there are 1000 subunits and each complete capsid has 60 subunits. Variation of the final mass fraction of complete capsids, f_c, is shown in (b)-(d): (b) variation with $C_0 = 0.11$ and $\theta_m = 0.5$, (c) variation with C_0 at several values of ε_b with $\theta_m = 0.5$, and (d) variation with θ_m for several values of ε_b and $C_0 = 0.11$. Note that ε_b does not denote the free energy to bind; there is a significant entropy penalty, calculated in Eq. 15.

energy, ε_b, upon binding, but subunits also face an entropic penalty, which depends on the number of bonds and the local bonding network.

The free energy for making a single bond to form a dimer can be determined by calculating the ratio of the partition functions for two bound subunits and two free subunits [35, 36]

$$q_2/q_1^2 = \frac{1}{8\pi^2} \int d\mathbf{R}_2 \int d\mathbf{\Omega}_2 \qquad (13)$$
$$\exp\left[-\beta u(\mathbf{R}_1, \mathbf{R}_2, \{\mathbf{b}_1\}, \{\mathbf{b}_2\})\right] H(1,2)$$

where u is defined in Eq. 2, $\mathbf{\Omega}_2$ describes the Euler angles of subunit 2, which specify the set of bond vector orientations, $\{\mathbf{b}_2\}$, and $H(1,2)$ is unity when $u(\mathbf{R}_1, \mathbf{R}_2, \{\mathbf{b}_1\}, \{\mathbf{b}_2\}) < -2k_BT$, and zero otherwise. In other words, we define two capsomers as bound if their potential energy of interaction is lower than $-2k_BT$. The free subunits are taken to be at a standard state with unit density and free rotation, and the coordinate system is centered on $\mathbf{R}_1$.

Expansion of $u(1,2)$ to quadratic order in each coordinate about the minimum in the potential gives

$$\Delta G_2 = -k_BT \ln q_2/q_1^2 = -\varepsilon_b - Ts_b \qquad (14)$$

with

$$s_b/k_B \approx -\frac{3}{2} \ln \left. \frac{2\pi\beta\partial^2 u_{att}(r)}{\partial r^2} \right|_{r=0} + \frac{1}{2} \ln \frac{2\beta\varepsilon_b^3\pi^7}{\theta_m^4\phi_m^2} \qquad (15)$$

where the two terms represent translational and rotational entropy, respectively. This result is compared to binding free energies calculated with Monte Carlo simulations in Fig. 3.

While there are many possible capsid structures consistent with most larger values of n, there is only one structure consistent with a complete capsid, which has $n = N_c$ subunits ($N_c = 60$ for the capsids studied in this work). The fact that misformed capsids and intermediates are generally not observed implies that ΔG_n is sharply peaked at $n = N_c$; defects that lead to larger or smaller capsids are unfavorable. There is a threshold density, ρ_{cc}, at which the fraction of subunits in capsids becomes significant [3, 37, 38, 39]

$$\ln \rho_{cc}a^3 \approx \beta\Delta G_{N_c}/N_c. \qquad (16)$$

By analogy with Eq. 14, the free energy of a complete capsid can be written as

$$\Delta G_{N_c} = -N_c n_b \varepsilon_b/2 - T(N_c - 1)s_b(n_b), \qquad (17)$$

where $s_b(n_b)$ is the entropy penalty for a subunit in a complete capsid, where each subunit has n_b bonds. If we neglect the

dependence of the entropy penalty on the number of bonds [i.e. assume $s_b(n_b) \approx s_b$], we can use Eqs. 15, 16, and 17 to calculate ρ_{cc}. Values of ρ_{cc} for capsid design B_3 ($n_b = 3$) with $\phi_m = \pi$ (the value used for all dynamical simulations with this work) are shown in Fig. 4, and are compared to kinetic assembly results in Fig. 6.

IV. KINETICS OF CAPSID ASSEMBLY

Capsid formation rate curves are sigmoidal. We have considered capsid assembly dynamics for design B_3 (see Figs. 1 and 2) over ranges of subunit concentrations, C_0 (reported in dimensionless units, $C_0 = N\sigma^3/L^3$), binding energies, ε_b, and maximum binding angles θ_m. The results we present use $\phi_m = \pi$; the effect of varying ϕ_m is similar to, but less dramatic than that of varying θ_m. Dynamics of different capsid designs are discussed below.

The fraction of subunits in completed capsids, f_c, is shown as a function of time for several binding energies in Fig. 5a. In all cases for which significant assembly occured, the rate of capsid formation has a roughly sigmoidal shape. This is a general feature of assembly reactions [20] that can be understood as follows. There is an initial lag phase during which capsid intermediates form and progress through the assembly cascade, followed by a rapid growth phase during which these intermediates assemble into complete capsids. Finally, growth slows when monomers (free subunits) are depleted and the remaining capsid intermediates are unable to bind with each other.

Final capsid yields are non-monotonic with respect to parameter values, but high yields are possible. The fraction of subunits in complete capsids, f_c, at the final observation time, $t = 6 \times 10^5$, is shown in Fig 5. As C_0, ε_b, or θ_m increase, intermediates form and grow more rapidly, and thus capsid yields increase to as high as 90%, meaning 15 of the 16 possible capsids were completed. One of the primary results of this study is that a particle model that does not include details such as heterogeneous nucleation or conformational changes can predict such high capsid yields.

Although capsids form more quickly as parameter values are increased, saturation of growth also occurs sooner and capsid yields are non-montonic in each parameter. The sensitivity of capsid yields to parameters seen in Fig. 5 is further illustrated with a kinetic phase diagram in Fig. 6. It demonstrates the coupled dependencies of capsid yields on system parameters. Phases are partitioned according to whether or not there is significant assembly, arbitrarily chosen as $f_c \geq 30\%$.

The non-monotronic variation of capsid yields with parameter values arises due to competition between faster capsid growth and kinetic traps. The initial steps in the assembly cascade result in the formation of fewer bonds than later steps. If the attractive energy of these bonds is not sufficient to overcome entropic loss the initial steps are uphill on a free energy barrier and hence, are slow. For parameter sets that are near ρ_{cc} (see Fig. 4), where half of the subunits are in complete capsids at equilibrium, the fact that a complete capsid has many more bonds than initial assembly products

indicates that the free energy barrier must be many times the thermal energy, $k_B T$. Significant assembly, therefore, does not occur within the finite assembly times we consider until parameter values are much higher than the thermodynamic critical values, and we identify a kinetic lower critical surface (LCS) in Fig. 6 that bounds the regions with significant assembly from below and to the left. We consider results at finite observation times because capsid assembly reactions are limited in-vivo by proteolysis times and in-vitro by experimental observation times.

Increasing parameters increases the overall rate of capsid growth: higher subunit concentrations, C_0, result in more frequent subunit collisions, higher values of θ_m increase the likelihood of binding upon a collision, and higher values of the binding energy, ε_b, decrease the rate of the reverse reaction (subunit unbinding). As parameter values cross the LCS, faster capsid growth leads to significant capsid yields, as seen in Fig. 5. At even higher values, however, assembly becomes frustrated by two kinetic traps (see Fig. 7) and we identify an upper critical surface (UCS) in Fig 6 to the top and right of the regions in which assembly is kinetically accessible. Because of these kinetic traps, assembly only occurs at subunit-subunit binding energies that are much smaller than values calculated from atomistic potentials in Ref. 21 (see Table 1 of that Ref.). When the binding entropy (see Eq. 15) is included, however, the resulting free energies are consistent with association constants fit to assembly experiments with Hepatitis B capsids in Ref. [40].

We present results at three observation times to show how the distance between assembly boundaries expands in all directions as time increases. The rough boundary of the kinetically accessible region in Fig. 6 is a measure of the statistical uncertainty that results because each data point describes a single stochastic trajectory. For trajectories run with different random number seeds at a given set of parameter values, the final number of complete capsids typically did not vary by more than one capsid; however, variations during the rapid growth phase were larger.

The kinetic trap depicted in Fig 7a arises when progress through initial assembly steps is too rapid, allowing so many capsids to initiate that the pool of monomers and small intermediates becomes depleted before a significant number of capsids are completed. If the remaining partial capsids have non-complementary geometries, further binding can only proceed upon disassembly. This kinetic trap has been seen in experiments [12] and predicted theoretically [17]; this theory, however, assumes that only monomers can add to partial capsids. As discussed below, binding of capsid intermediates is an important mode of assembly and growth does not become frustrated until only intermediates with non-complementary geometries remain.

The kinetic trap just described may not limit assembly *in vivo*, where there is a continual supply of new capsid proteins. Subunit bonding in configurations not consistent with a complete capsid (misbonding), however, can lead to a kinetic trap that could frustrate assembly even with an unlimited supply of subunits. It is not surprising that misbonding occurs more frequently as θ_m increases, since there is a smaller driv-
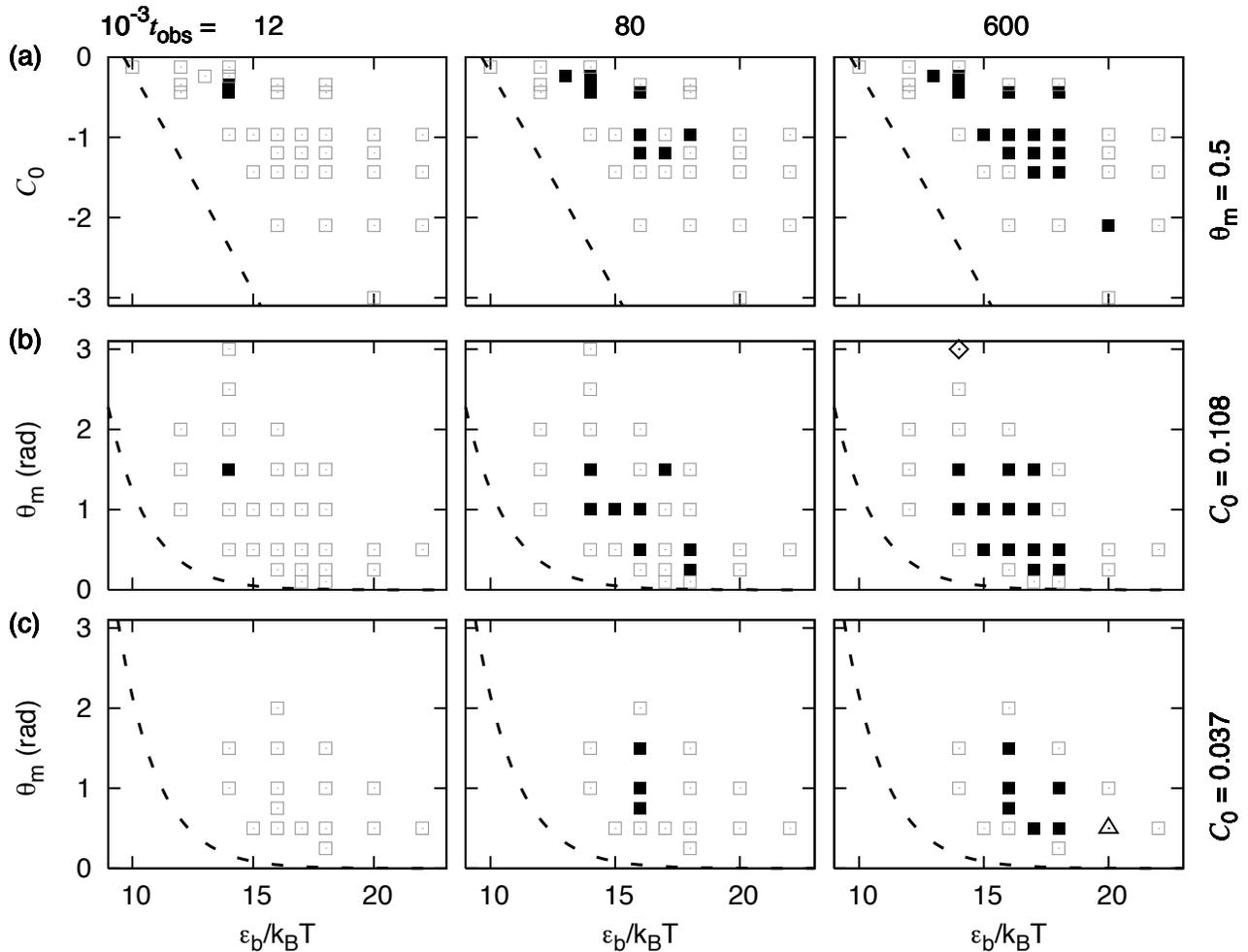
FIG. 6: Changing model parameters reveals the kinetic phase diagram for design B_3. Filled points denote parameter values for which 30% of subunits are in complete capsids ($f_c \geq 30\%$) by the observation time, t_{obs}, open points indicate parameter values for which $f_c < 30\%$, and the dashed lines indicate the location of the thermodynamic critical surface, calculated with Eq. 16. The first, second, and third columns correspond to observation time $t_{obs} = 1.2 \times 10^4$, 8×10^4, and 6×10^5, respectively. The top row (a) shows cross-sections through C_0 and ε_b with $\theta_m = 0.5$. The second and third row show cross-sections through θ_m and ε_b, with (b) $C_0 = 0.11$ and (c) $C_0 = 0.037$. In each case the region covered by filled points roughly defines a cross-section of parameter space within which assembly is kinetically possible. Simulation snapshots corresponding to the $\diamond$ in the right hand panel in row (b) and the $\triangle$ in the right hand panel in row (c) are shown in Fig. 7.

ing force toward the minimum energy orientation. As noted by Berger and co-workers [26], though, increasing concentration and binding energy can stabilize subunits with strained bonds, and the higher rate of capsid growth under these conditions can cause misbonded subunits to become trapped in a growing capsid by further addition of subunits. Because so many assembly pathways that do not lead to complete capsids are available at these parameter values, the minimum energy configuration, with complete capsids, is seldom realized and misformed capsids with spiraling or multi-shelled configurations dominate, as shown in Fig. 7b. Progression from this state to a completed capsid is extremely slow because breakage of many bonds is required. It would be difficult to assess the importance of configurations such as that shown in Fig. 7b with models that have assumed assembly pathways.

B_5 capsids grow primarily through additions of individ-

ual subunits, while combination of clusters is essential for assembly of B_4 and B_3 capsids. The variations of final capsid yields with ε_b for the capsid designs B_3, B_4, and B_5 (see Fig 2) are shown in Fig 8a. Although assembly occurs within different ranges of ε_b for each design, assembly kinetics within these ranges are similar, as shown in Fig 8b. In addition, the optimal assembly ($f_c \approx 0.9$) for each design occurs at approximately the same value of $n_b\varepsilon_b \approx 50$, meaning that the complete capsids all have about the same stability. Variation of assembly with C_0 and θ_m (not shown) is also similar for each design.

Although the capacity to assemble spontaneously is similar for each capsid design, the mechanism of assembly (near optimal assembly) for B_5 is qualitatively different from that for B_4 and B_3. We evaluated assembly mechanisms from simulations by tabulating the size, n_{be}, of the smallest intermediate in-
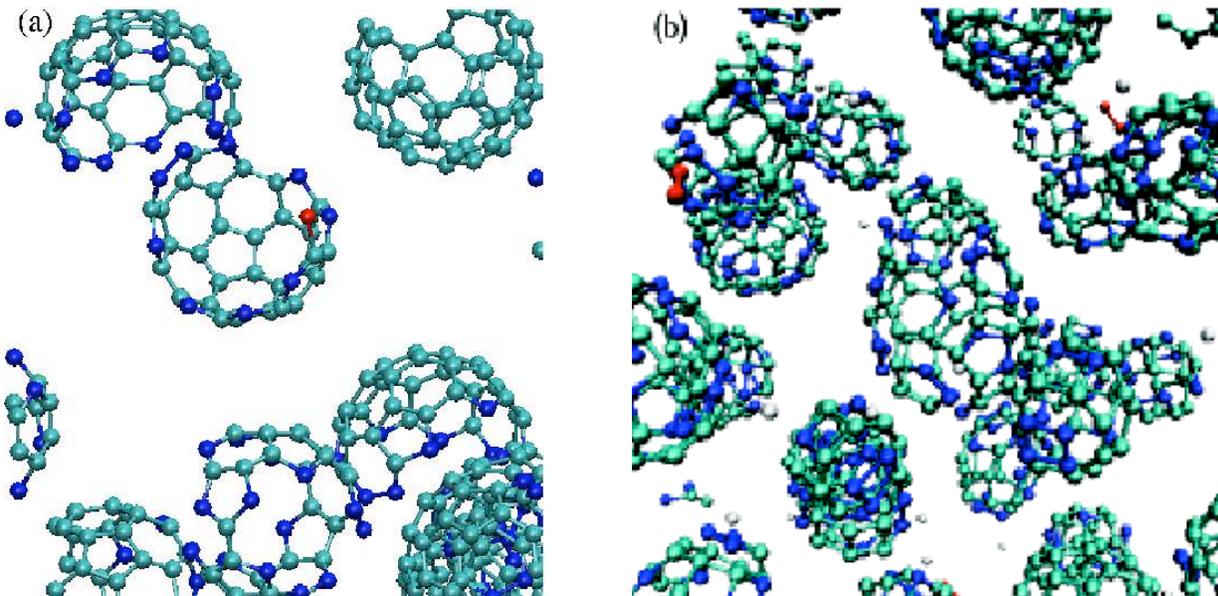
FIG. 7: Snapshots corresponding to unassembled points in Fig. 6, which illustrate the two kinetic traps described in the text. (a) Parameter values corresponding to the $\diamond$ in Fig. 6 allowed rapid capsid initiation and growth, which depleted monomers and small intermediates before capsids were completed. (b) At parameter values corresponding to the $\triangle$, strained bonds are incorporated into growing capsids. These snapshots have zoomed in on a representative portion of the system to aid visibility. Subunit colors indicate the number of bonds: white = 0, red = 1, turquoise = 2, and dark blue = 3 bonds.

volved in each binding or unbinding event (see Appendix B). The net contribution to capsid growth by intermediates of size n_{be}, $b_{net}(n_{be})$, is shown for each capsid design in Fig 9. While about 33% of subunits assembled as multimers ($n_{be} > 1$) for B_3 and B_4 capsids, multimer binding accounted for only 6% of all binding for B_5 capsids.

The influence of capsid design on mechanism can be understood by examining assembly pathways that are available if growth occurs only through monomer additions, such as those shown in Fig. 10. Once dimerization occurs for B_5, all subsequent monomers can add in such a way that two or more bonds are formed. For parameters values at which optimal assembly occurs, the formation of a single bond is unfavorable due to entropy loss, but the formation of two or more bonds is favorable. Consequently, the approximate projection of free energy onto cluster size (see Appendix C) shown in Fig. 11 is monotonically decreasing after formation of a dimer.

For architectures B_3 and B_4, it is not possible to construct an assembly path for which monomers form multiple bonds at all cluster sizes greater than two (see Fig. 10). Therefore, free energy profiles consistent with these architectures, shown in Fig. 11, have numerous free energy barriers and local minima. At parameter values that are optimal for B_5 assembly, progression of B_4 and B_3 intermediates through the assembly cascade is stymied by these free energy barriers.

All free energy barriers vanish if parameters are increased until formation of single bonds is favorable. Since dimers are stable under these conditions, however, too many capsids initiate and the system becomes mired in the kinetic trap shown in Fig. 7a. At moderate parameter values, B_4 intermediates that correspond to local minima, such as trimers and hexam-

ers, are metastable. Optimal assembly occurs when these intermediates bind to growing capsids as fast as they are formed. The first local minimum for B_3 capsids does not occur until a cluster size of five; in this case, optimal assembly occurs at parameter values for which dimerization is only slightly unfavorable and binding events involving dimers are common (see Fig. 9). As parameter values are increased beyond optimal assembly conditions, formation of small intermediates becomes more rapid and multimer binding becomes more important for all capsid designs.

Note that these free energies compare the relative stability of different multimers. There are also free energy barriers not shown that are associated with subunit binding or unbinding, which is required to transition between these states.

Given the importance of multimer binding to assembly of some capsid designs, it might seem surprising that a rate equation model [17, 20] that assumes capsids grow only via addition of monomers predicts significant assembly for some parameter values. That particular class of models assumes, however, that monomers bind to intermediates with an average binding free energy, independent of the number of intersubunit contacts formed in a particular configuration. While not explicitly described herein, we have considered a model in which binding free energies were specifically calculated for each capsid intermediate, but the assumption that only monomers could bind to these intermediates was retained. The assembly dynamics predicted by this model for B_5 were consistent with those seen in Brownian dynamics simulations, but concentrations of intermediates at local free energy minima built up for B_4 and B_3 designs, as well as for the design shown in Fig 1B of Ref. 20. Because these intermediates
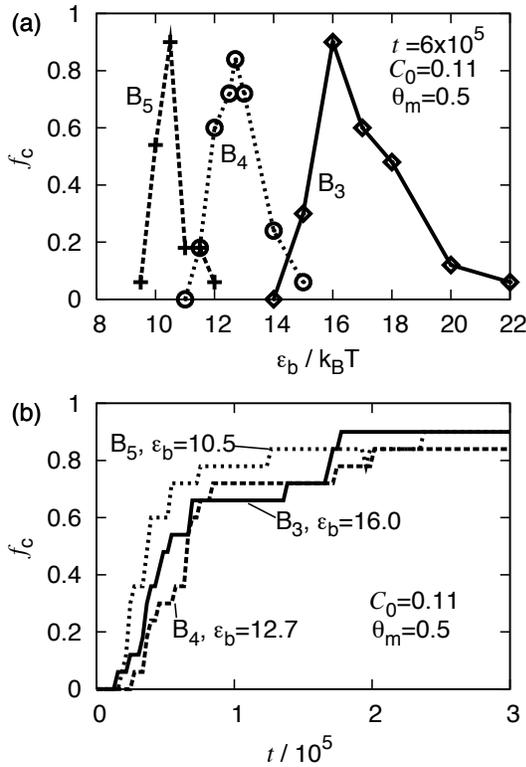
FIG. 9: B_5 capsids grow primarily through additions of individual subunits, while binding of multimers to growing capsids is essential for assembly of B_4 and B_3 capsids. The fraction of binding, b_{net} (see Appendix B), for each cluster sizes n_{be} is shown for each design, and the total binding contribution for multimers, $b_{mult} = \sum_{n_{be}>1} b_{net}(n_{be})$, is shown in the inset. Statistics were measured for the parameters used in Fig. 8 through $t = 2.25 \times 10^5$, by which time the majority of assembly was completed for these parameter values.

FIG. 8: Assembly kinetics are similar for each capsid design, B_3, B_4, and B_5. (a) The final capsid yields, f_c at $t_{obs} = 6 \times 10^5$, are shown versus binding energy for each capsid design for $C_0 = 0.11$ and $\theta_m = 0.5$. (b) The assembly time series are shown for the optimal values of ε_b from (a) ($\varepsilon_b = 16.0$ for B_3, 12.7 for B_4, and 10.5 for B_5).

FIG. 10: (a) Examples of the assembly pathways that are available if only monomers can add to growing capsids. Once a B_5 dimer is formed, subsequent monomers can always form two or more bonds, whereas all assembly paths for B_3 and B_4 require formation of single bonds. (b) One example of a multimer binding step for design B_4 that avoids formation of single bonds.

could not bind with each other, the predicted assembly was much less efficient than that predicted by Brownian dynamics simulations. These results suggest that it may be important to consider binding of complexes that are larger than the basic assembly unit when hypothesizing assembly mechanisms from experimental data.

For many viruses, the basic assembly units are believed to be small intermediates, such as dimers or trimers. Experimentally observed high concentrations of these species during assembly reactions imply that they form rapidly and are extremely metastable. This feature could be included in our model by designing a new "subunit" that represents the basic assembly unit, or by choosing higher binding energies for certain bond vectors. In this work, where all maximum binding energies are equal, the importance of multimer binding for B_4 and B_3 capsids is not a result of the interaction between individual subunits. Rather, the collective interactions of many subunits lead to a free energy profile with numerous local minima, which forces assembly to proceed through binding of intermediates. Although binding of trimers and other multimers is essential to B_4 assembly in our simulations, the fraction of subunits that comprise these intermediates is always small compared to the fraction of subunits that are monomers or in completed capsids (see Fig. 12). Hence, the signifi-
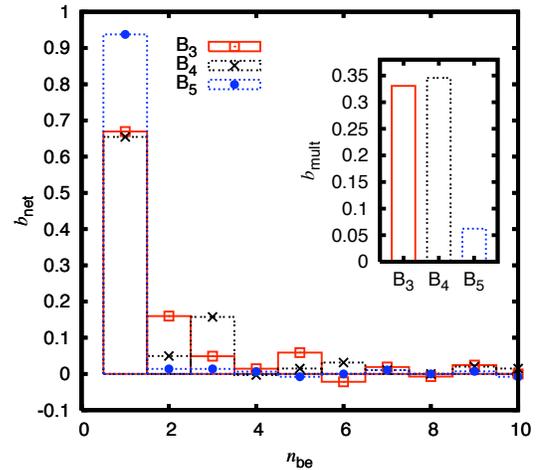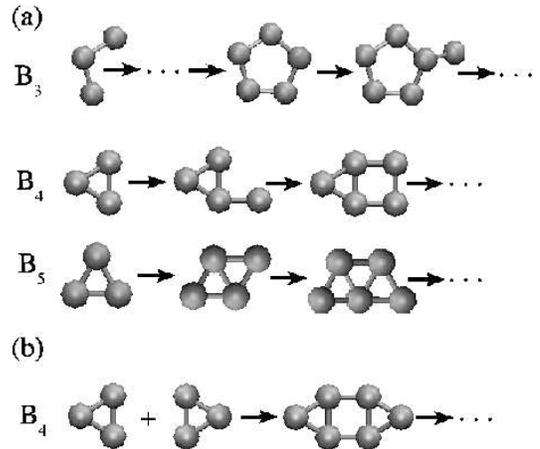
cance of binding of multimers would be difficult to detect by bulk experiments, such as light scattering or size exclusion chromatography, alone. The combination of these techniques, though, with selective deletion of residues through mutation [41] or single molecule experiments may offer insights into the importance of various intermediates in capsid assembly.

Capsids are metastable in infinite dilution and capsid disassembly shows hysteresis. Since even single virions can sometimes infect cells, viral capsids must be metastable in in-
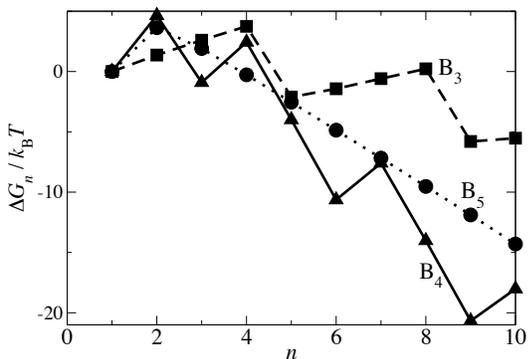
FIG. 11: Free energy projections onto the number of particles in a capsid, n, for each design, relative to monomers in solution at $C_0 = 0.11$ with $\theta_m = 0.5$. The values of ε_b are the optimal values from Fig. 8, 16.0, 10.5, and 12.7 for the B_3, B_4, and B_5 designs, respectively. Free energies were obtained with Boltzmann weighted sums over configurations with a given cluster size as described in Appendix C. Lines are drawn between the points as a guide to the eye.
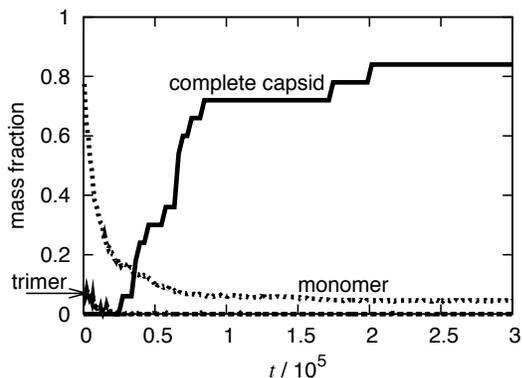

FIG. 12: The mass fraction of monomers, trimers, and complete capsids (60 subunits, with $n_b = 4$ bonds each) as a function of time, t, for design B_4, illustrating that intermediate concentrations are always small during successful assembly. The parameters are those given in Fig 8.

finite dilution. Model capdsids also displayed this feature; for example, significant assembly with $C_0 = 0.008$ did not occur for $\varepsilon_b < 20.0$ (see Fig. 6), but isolated complete capsids simulated without periodic boundary conditions (to model infinite dilution) were metastable through $t = 6 \times 10^5$ for $\varepsilon_b \geq 14.0$. This result indicates that the final yield of the capsids at some binding energies will be different for a trajectory that started with mostly complete capsids then for a trajectory that started with random subunit configurations, as shown in Fig 13. In other words, there would be hysteresis between assembly and disassociation.

Hysteresis arises because, as discussed above, there can be large free energy barriers separating the early stages of assembly, where there are few bonds per subunit, and complete capsids, for which each subunit has n_b bonds. Therefore, monomers (or complete capsids) can be metastable throughout a finite length trajectory above (or below) ρ_{cc}. Once the
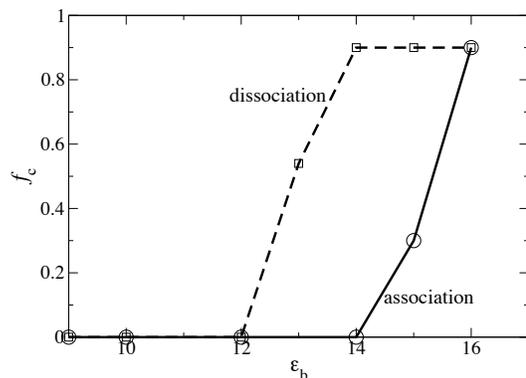

FIG. 13: Capsid yeilds as a function of ε_b (or equivalently inverse temperature or inverse denaturant concentration) illustrating hysteresis between association and dissociation of capsids. The final capsid yields, f_c at $t_{obs} = 6 \times 10^5$, are shown for simulations started with subunits in random configurations (association) and simulations started with the final configuration from the B_3 simulation shown in Fig. 8, which had $f_c = 0.9$ (dissociation). Parameter values were $C_0 = 0.11$ and $\theta_m = 0.5$.

first subunit is removed from a metastable complete capsid, neighboring subunits have fewer bonds and further disassembly is rapid. Hysteresis in capsid assembly–disassembly has been seen with experiments and theory by Zlotnick and coworkers [13].

V. CONCLUSIONS AND OUTLOOK

In this work we examined ensembles of assembly trajectories for models that assemble into capsid-like objects. We demonstrated that computational models can distinguish driving forces and corresponding mechanisms that lead to successful assembly from those that engender dynamic frustration. Therefore, the approach we have outlined might be used to good effect to analyze the dynamics of other assembly models (e.g., [6, 23, 26, 28]). as well as that for other types of assembly models. In addition to the calculations presented herein, there are other ways that ensembles of assembly trajectories can be carefully analyzed. For instance, distributions of capsid formation times could be studied by simulation and potentially estimated with single molecule experiments; comparisons could shed light on assembly mechanisms, such as the mechanisms for B_4 and B_5 assembly illustrated in this work. Trajectories generated by the approach described in this work can be a starting point for performing importance sampling in trajectory space [42, 43, 44], which would facilitate statistical analysis of ensembles of assembly pathways.

Rechtsman and co-workers describe an "inverse statistical mechanical-methodology" that allows importance sampling in model space to design potentials that direct assembly into a particular ground state [45]. The ability to generate ensembles of dynamical trajectories invites a related strategy, in which one seeks to optimize a function of entire assembly paths, such as capsid assembly times or identities of key intermediates. This approach would involve importance

sampling steps in trajectory space, such as shooting moves [46], as well as sampling steps in model space. Understanding model features that lead to specific assembly behavior could guide and interpret experiments that involve mutated capsid proteins.

APPENDIX A

The equations of motion given in Eq. 8 were integrated as follows. Translational displacements are calculated as described in Eq. 7 of Ref. 32. Bond vector orientations are specified in body fixed coordinates at the beginning of the simulations. The space fixed coordinates, $\{\mathbf{b}^{(\alpha)}(t)\}$, are determined from a rotation matrix, $\mathbf{A}(t)$, which is evolved in time using quaternions, which satisfy the equation of motion given in Eq. 3.37 of Ref. 31. This equation requires angular velocities, $\boldsymbol{\omega}$, which are determined in an analogous fashion to the translational displacements

$$\boldsymbol{\omega}_i = \gamma_{\mathrm{r}}/2\left(\boldsymbol{\tau}_i^a + \boldsymbol{\tau}_i^b\right) + \delta\boldsymbol{\tau}_i \tag{A1}$$

where the torques are calculated at two points

$$\begin{aligned}\boldsymbol{\tau}_i^a(t) &\equiv \boldsymbol{\tau}_i\left(\{\mathbf{R}_i(t), \mathbf{b}(t)\}\right)\\ \boldsymbol{\tau}_i^b(t) &\equiv \boldsymbol{\tau}_i\left(\{\mathbf{R}_i^b(t), \mathbf{b}^b(t)\}\right)\end{aligned} \tag{A2}$$

with the predictor positions determined as in Ref. 32

$$\mathbf{R}_i^b = \mathbf{R}_i + \delta t\left(\gamma\mathbf{F}_i + \delta\mathbf{F}_i\right). \tag{A3}$$

The predictor bond orientations, $\{\mathbf{b}^b(t)\}$, are determined from a predictor rotation matrix, which is calculated from Eq. 3.37 of Ref. 31, using predictor angular velocities calculated as

$$\boldsymbol{\omega}_i^b = \gamma_{\mathrm{r}}\boldsymbol{\tau}_i^a + \delta\boldsymbol{\tau}_i. \tag{A4}$$

This formulation assumes that subunits are hydrodynamically isolated and that rotational and translational sources of friction are not coupled; these assumptions can be relaxed as in Ref. 47.

APPENDIX B

The contribution of multimer-binding to the final assembly product was calculated from simulations as follows. Multi-mers were designated by clustering subunits connected by one or more bonds. A binding event occurred when the size of a cluster changed, either through a combination of two clusters (positive binding) or division of a cluster (negative binding). Cluster sizes were output every 10 steps; more than one binding event involving the same cluster within 10 steps was found to be exceptionally rare. The size of a binding event, n_{be}, was defined by the size of the smallest reactant cluster for positive binding or the smallest product cluster for negative binding. The net forward binding due to events of size n_{be} is given by

$$b_{\mathrm{net}}(n_{\mathrm{be}}) = n_{\mathrm{be}}\left(b_+(n_{\mathrm{be}}) - b_-(n_{\mathrm{be}})\right) \tag{B1}$$

where b_+ and b_- are the number of positive and negative binding events of size n_{be}, respectively.

APPENDIX C

The free energy, Δg_i, to build a particular capsid configuration, i, from a bath of subunits at concentration C_0, can be determined by analogy to Eq. 14 if the dependence of binding entropy on the number of bonds is neglected

$$\Delta g_i = \sum_{j=1}^{n_i} [-b_j\varepsilon_{\mathrm{b}}/2] - (n_i-1)T\left[k_{\mathrm{B}}\ln(\pi\sigma^3 C_0/6) + s_{\mathrm{b}}(1)\right], \tag{C1}$$

where j sums over each subunit in the capsid, n_i is the number of subunits in configuration i, and b_j is the number of bonds for subunit j. We project the free energy onto the number of particles in a capsid, n, by summing over configurations containing n of subunits

$$G_n = -k_{\mathrm{B}}T\ln\sum_i \delta_{n_i,n}\exp\left(-\beta\Delta g_i\right). \tag{C2}$$

We performed this sum with Monte Carlo simulations in which trial capsid configurations were generated by adding or deleting subunits from current configurations, and then accepted or rejected according to the Metropolis [48] criterion, with the Boltzmann distribution given by Eq. C1. Only configurations consistent with minimum energy bonding were considered; thus, this approach was only applicable for parameters with which misformed capsids do not occur. The average free energy for capsids of size n was efficiently calculated by carrying out umbrella sampling [34] in which a harmonic potential as a function of capsid size was used to bias the number of subunits in the capsid.

[1] Crick, F. H. C., and J. D. Watson. 1956. Structure of small viruses. *Nature (London)* 177:473–5.

[2] Caspar, D. L. D., and A. Klug. 2004. Physical principles in

the construction of regular viruses. *Cold Spring Harbor Symp. Quant. Biol.* 4:1407–1413.

[3] Bruinsma, R. F., W. M. Gelbart, D. Reguera, J. Rudnick, and R. Zandi. 2003. Viral self-assembly as a thermodynamic process. *Phys. Rev. Lett.* 90:248101.

[4] Zandi, R., D. Reguera, R. F. Bruinsma, W. M. Gelbart, and J. Rudnick. 2004. Origin of icosahedral symmetry in viruses. *Proc. Natl. Acad. Sci. USA* 101:15556–15560.

[5] Twarock, R. 2004. A tiling approach to virus capsid assembly explaining a structural puzzle in virology. *J. Theor. Biol.* 226:477–482.

[6] Chen, T., Z. Zhang, and S. C. Glotzer. 2005. A universal precise packing sequence for self-assembled convex structures. *preprint* .

[7] Fraenkel-Conrat, H., and R. C. Williams. 1955. Reconstitution of active tobacco mosaic virus from its inactive protein and nucleic acid components. *Proc. Natl. Acad. Sci. USA* 41:690–698.

[8] Butler, P. J., and A. Klug. 1978. The assembly of a virus. *Sci. Am.* 329:62.

[9] Klug, A. 1999. The tobacco mosaic virus particle: structure and assembly. *Phil. Trans. R. Soc. Lond. B* 354:531–535.

[10] Fox, J. M., J. E. Johnson, and M. J. Young. 1994. RNA/protein interactions in icosahedral virus assembly. *Seminars in Virology* 5:51–60.

[11] Zlotnick, A., N. Cheng, J. F. Conway, F. P. Booy, A. C. Steven, S. J. Stahl, and P. T. Wingfield. 1996. Dimorphism of hepatitis B virus capsids is strongly influenced by the c-terminus of the capsid protein. *Biochemistry* 35:7412–7421.

[12] Zlotnick, A., R. Aldrich, J. M. Johnson, P. Ceres, and M. J. Young. 2000. Mechanism of capsid assembly for an icosahedral plant virus. *Virology* 277:450–456.

[13] Singh, S., and A. Zlotnick. 2003. Observed hysteresis of virus capsid disassembly is implicit in kinetic models of assembly. *J. Biol. Chem.* 278:18249–18255.

[14] Willits, D., X. Zhao, N. Olson, T. S. Baker, A. Zlotnick, J. E. Johnson, T. Douglas, and M. J. Young. 2003. Effects of the Cowpea chlorotic mottle bromovirus β-hexamer structure on virion assembly. *Virology* 306:280–288.

[15] Casini, G. L., D. Graham, D. Heine, R. L. Garcea, and D. T. Wu. 2004. In vitro papillomavirus capsid assembly analyzed by light scattering. *Virology* 325:320–327.

[16] Valegard, K., J. B. Murray, N. J. Stonehouse, S. van den Worm, P. G. Stockey, and L. Lijlas. 1997. The three-dimensional structures of two complexes betweeen recombinant MS2 capsids and RNA operator fragments reveal sequence-specific protein-RNA interactions. *J. Mol. Biol* 270:724–738.

[17] Zlotnick, A. 1994. To build a virus capsid. An equilibrium model of the self assembly of polyhedral protein complexes. *J. Mol. Biol.* 241:59–67.

[18] Berger, B., P. W. Shor, L. Tucker-Kellogg, and J. King. 1994. Local rule-based theory of virus shell assembly. *Proc. Natl. Acad. Sci. USA* 91:7732–7736.

[19] Zlotnick, A., J. M. Johnson, P. W. Wingfield, S. J. Stahl, and D. Endres. 1999. A theoretical model successfully identifies features of hepatitis B virus capsid assembly. *Biochemistry* 38:14644–14652.

[20] Endres, D., and A. Zlotnick. 2002. Model-based analysis of assembly kinetics for virus capsids or other spherical polymers. *Biophys. J.* 83:1217–1230.

[21] Reddy, V., H. A. Giesing, R. T. Morton, A. Kumar, C. B. Post, C. L. Brooks 3rd, and J. E. Johnson. 1998. Energetics of quasiequivalence: computational analysis of protein-protein interactions in icosahedral viruses. *Biophys. J.* 1998:546–558.

[22] Keef, T., C. Micheletti, and R. Twarock. 2005. Mas-ter equation approach to the assembly of viral capsids. arXiv:q-bio.BM/0508030 v1.

[23] Rapaport, D. C. 2004. Self-assembly of polyhedral shells: a molecular dynamics study. *Phys. Rev. E.* 70:051905.

[24] Berger, B., J. King, R. Schwartz, and P. W. Shor. 2000. Local rule mechanism for selecting icosahedral shell geometry. *Discrete Applied Mathematics* 104:97–111.

[25] Schwartz, R., R. L. Garcea, and B. Berger. 2000. "Local rules" theory applied to polyomavirus polymorphic capsid assemblies. *Virology* 268:461–470.

[26] Schwartz, R., P. W. Shor, P. E. J. Prevelige, and B. Berger. 1998. Local rules simulation of the kinetics of virus capsid self-assembly. *Biophys. J.* 75:2626–2636.

[27] Rapaport, D. C., J. E. Johnson, and J. Skolnick. 1999. Supramolecular self-assembly: molecular dynamics modeling of polyhedral shell formation. *Comput. Phys. Comm.* 121:231–235.

[28] Zhang, Z., and S. C. Glotzer. 2004. Self-assembly of patchy particles. *Nano Letters* 4:1407–1413.

[29] Xie, Q., and M. S. Chapman. 1996. Canine parvovirus capsid structure, analyzed at 2.9 Å resolution. *J. Mol. Biol.* 264:497–520.

[30] Andersen, H. C., D. Chandler, and J. D. Weeks. 1972. Roles of repulsive and attractive forces in liquids: the optimized random phase approximation. *J. Chem. Phys.* 56:3812–3823.

[31] Allen, M. P., and D. J. Tildesley. 1987. Computer Simulation of Liquids. Oxford University Press, New York.

[32] Branka, A. C., and D. M. Heyes. 1999. Algorithms for Brownian dynamics computer simulations: Multivariable case. *Phys. Rev. E.* 60:2381–2387.

[33] Heyes, D. M., and A. C. Branka. 2000. More efficient Brownian dynamics algorithms. *Mol. Phys.* 98:1949–1960.

[34] Chandler, D. 1987. Introduction to Modern Statistical Mechanics. Oxford University Press, New York.

[35] Erickson, H. P., and D. Pantaloni. 1981. The role of subunit entropy in cooperative assembly: Nucleation of microtubules and other two-dimensional polymers. *Biophys. J.* 34:293–309.

[36] Ben-tal, N., B. Honig, C. Bagdassarian, and A. Ben-Shaul. 2000. Association entropy in adsorption processes. *Biophys. J.* 79:1180–1187.

[37] A., B.-S., and W. M. Gelbart. 1994. *In* Micelles, Membranes, Microemulsions, and Monolayers, W. M. Gelbart, A. Ben-Shaul, and D. Roux, editors, chapter 1. Springer-Verlag, New York.

[38] Maibaum, L., A. R. Dinner, and D. Chandler. 2004. Micelle formation and the hydrophobic effect. *J. Phys. Chem. B* 108:6778–6781.

[39] Kegel, W. K., and P. van der Schoot. 2004. Competing hydrophobic and screened-coulomb interactions in hepatitis B virus capsid assembly. *Biophys. J.* 86:3905–3913.

[40] Ceres, P., and A. Zlotnick. 2002. Weak protein-protein interactions are sufficient to drive assembly of hepatitis B virus capsids. *Biochemistry* 41:11525–11531.

[41] Reguera, J., A. Carreira, L. Riolobos, J. M. Almendral, and M. G. Mateu. 2004. Role of interfacial amino acid residues in assembly, stability, and conformation of a spherical virus capsid. *Proc. Natl. Acad. Sci. USA* 101:2724–2729.

[42] Dellago, C., P. G. Bolhuis, F. S. Csajka, and D. Chandler. 1998. Transition path sampling and the calculation of rate constants. *J. Chem. Phys.* 108:1964–1977.

[43] Bolhuis, P. G., D. Chandler, C. Dellago, and P. L. Geissler. 2002. Transition path sampling: Throwing ropes over rough mountain passes, in the dark. *Annu. Rev. Phys. Chem.* 53:291–318.

[44] E, W., W. Ren, and E. Vanden-Eijnden. 2005. Finite temperature string method for the study of rare events. *J. Phys. Chem. B* 109:6688–6693.

[45] Rechtsman, M., F. Stillinger, and S. Torquato. 2005. Optimized interactions for targeted self-assembly: Application to honeycomb lattice. arXiv:cond-mat/0508030 v1.

[46] Dellago, C., P. G. Bolhuis, and P. L. Geissler. 2001. Transition path sampling. *Adv. Chem. Phys.* 123:1–78.

[47] Dickinson, E., S. A. Allison, and J. A. McCammon. 1985. Brownian dynamics with rotation-translation coupling. *J. Chem. Soc., Faraday Trans. 2* 81:59–160.

[48] Metropolis, N., A. W. Rosenbluth, M. N. Rosenbluth, A. H. Teller, and E. Teller. 1953. Equation of state calculations by fast computing machines. *J. Chem. Phys.* 21:1087–1092.

[49] Humphrey, W., A. Dalke, and K. Schulten. 1996. VMD – Visual Molecular Dynamics. *Journal of Molecular Graphics* 14:33–38.